Atmospheric
Chemistry
and Physics

Revisiting the evolution of downhill thunderstorms over Beijing: a new perspective from a radar wind profiler mesonet

Xiaoran Guo[1,2]**, Jianping Guo**[1]**, Tianmeng Chen**[1]**, Ning Li**[1]**, Fan Zhang**[1]**, and Yuping Sun**[1]

[1]State Key Laboratory of Severe Weather, Chinese Academy of Meteorological Sciences,
Beijing 100081, China
[2]College of Earth and Planetary Sciences, University of Chinese Academy of Sciences,
Beijing 100049, China

Correspondence: Jianping Guo (jpguocams@gmail.com, jpguo@cma.gov.cn)

Abstract. Downhill thunderstorms frequently occur in Beijing during the rainy seasons, leading to substantial precipitation. The accurate intensity prediction of these events remains a challenge, partly attributed to insufficient observational studies that unveil the thermodynamic and dynamic structures along the vertical direction. This study provides a comprehensive methodology for identifying both enhanced and dissipated downhill thunderstorms. In addition, a radar wind profiler (RWP) mesonet has been built in Beijing to characterize the prestorm environment downstream of the thunderstorms at the foothill. This involves deriving vertical distributions of high-resolution horizontal divergence and vertical motion from the horizontal wind profiles measured by the RWP mesonet. A case study of an enhanced downhill thunderstorm on 28 September 2018 is carried out for comparison with a dissipated downhill thunderstorm on 23 June 2018, supporting the notion that a deep convergence layer detected by the RWP mesonet, combined with the enhanced southerly flow, favors the intensification of thunderstorms. Statistical analyses based on radar reflectivity from April to September 2018–2021 have shown that a total of 63 thunderstorm events tend to be enhanced when entering the plain, accounting for about 66 % of the total number of downhill thunderstorm events. A critical region for intensified thunderstorms lies on the downslope side of the mountains west to Beijing. The evolution of a downhill storm is associated with the dynamic conditions over the plain compared to its initial morphology. Strong westerly winds and divergence in the middle of troposphere exert a critical influence on the enhancement of convection, while low-level divergence may lead to dissipation. The findings underscore the significant role of an RWP mesonet in elucidating the evolution of a downhill storm.

1 Introduction

The complex evolution of convective systems crossing mountainous terrain represents a substantial forecasting challenge (Chu and Lin, 2000; Feng et al., 2019). It has been previously reported that downhill thunderstorms with intensive reflectivity and good organization are more likely to successfully be maintained or strengthened compared to isolated and small-scale thunderstorms (Castro et al., 1992). Various thermal factors that favor the development of downhill thunderstorms have been identified, including higher instability and lower convective inhibition (Letkewicz and Parker, 2010, 2011; Keighton et al., 2007), adequate water vapor accompanied by low-level jets (Tompkins, 2001; McCaul and Cohen, 2004; Weckwerth et al., 2014), and a cool pool (Teng et al., 2000; Jeevanjee and Romps, 2015; Li et al., 2017; Xiao et al., 2017). Furthermore, a few studies in the literature have demonstrated the importance of the dynamic environment over the plain, such as surface and lower-tropospheric convergence for convection initiation (Frame and Markowski,

2006; Miglietta and Rotunno, 2009; Wilson et al., 2010) and strong vertical wind shear (Parker and Ahijevych, 2007; Reeves and Lin, 2007; Xiao et al., 2019).

The topography in Beijing is intricate, given its location at the foot of the Taihang Mountains to the west and the Yan Mountains to the north, both of which have ridges with elevations exceeding 1200 m (Fig. 1a). Wilson et al. (2007) found that downhill thunderstorms, particularly those originating from the west, constituted 79 % of all thunderstorms in Beijing between 2003 and 2005, as determined through a statistical analysis of thunderstorm datasets. The distinctive topography and frequent occurrence of downhill thunderstorms in Beijing afford us an excellent opportunity to observe the inherent dynamic structures of downhill thunderstorms and their pre-storm environments. This, in turn, allows for a more in-depth investigation into the potential physical mechanisms underlying the formation of this severe weather event. However, most previous studies are limited to the analysis of a single downhill thunderstorm case (Chen et al., 2017; Sun and Cheng, 2017; Kang et al., 2019). Besides, the investigation of the pre-storm environment and the evolution process of thunderstorms are either based on model simulations (Chen and Lin, 2005; Xiao et al., 2015; Li et al., 2017) or reanalysis data (Wang et al., 2019), largely owing to the dearth of high-density continuous vertical profiling measurements of wind, temperature, and humidity.

Furthermore, there is no objective method that can be used to identify and track the propagation of downhill thunderstorms in the literature. Therefore, more urgent efforts are warranted to investigate the difficult-to-forecast storm type from a statistical perspective of ground-based atmospheric profiling mesonet observations. A high-density mesonet consisting of six radar wind profilers (RWPs) has been established in the Beijing since 2018 (Fig. 1b) to continuously observe three-dimensional wind fields with high temporal and vertical resolution. This provides us with a valuable tool to explore the atmospheric dynamic structures, such as areal-averaged vorticity, divergence, and vertical velocity, of the pre-storm environment for downhill thunderstorms by using the parameters derived from the RWP mesonet. The primary goals of this study are twofold: (1) to develop an objective method to identify the event of a downhill thunderstorm and its evolution, mainly based on composite radar reflectivity from weather radar, and (2) to explore the statistical patterns of downhill thunderstorms and reveal the dynamical structures in the development of downhill thunderstorms, aiming to attain a deeper understanding of the evolution processes of these thunderstorms.

The next section describes the data and methodology, in which a novel objective method is proposed to characterize the evolution of a downhill thunderstorm. Section 3 presents a case study of an enhanced downhill thunderstorm. Statistical analyses of the relationship are conducted in Sect. 4 between the wind profile, convergence, and the evolution
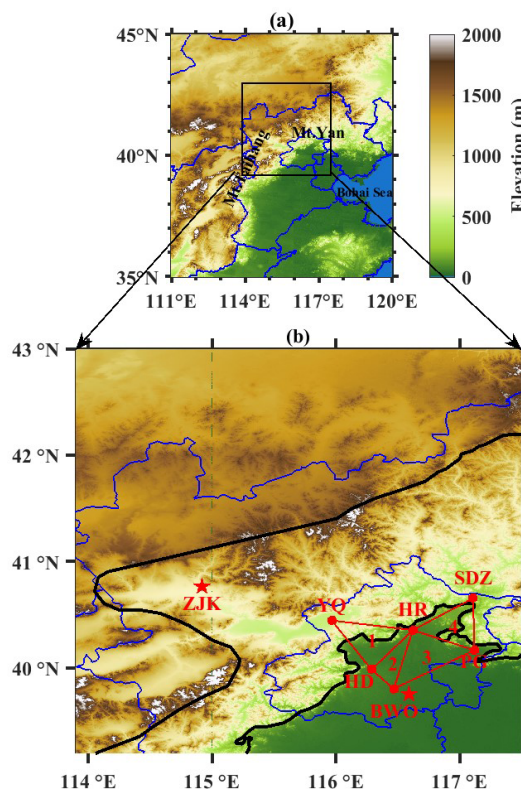
Figure 1. (a) Spatial distribution of the topography over northern China with the blue line denoting the provincial boundaries. The locations of the Taihang Mountains (Mt. Taihang), Yan Mountains (Mt. Yan), and Bohai Sea are written in black text. **(b)** Map of Beijing with six RWPs (red dots) deployed at Shangdianzi (SDZ), Huairou (HR), Yanqing (YQ), Haidian (HD), Pinggu (PG), and the Beijing Weather Observatory (BWO) and surrounding areas. The BWO and Zhangjiakou (ZJK) are deployed with an L-band radiosonde (red pentagrams). The four red triangles denote the areas used to calculate the horizontal divergence with the triangle method. The left black line marks the ridge line, and the right black line marks the plain line that denotes the 200 m terrain elevation.

of downhill thunderstorms. A summary and concluding remarks are given in Sect. 5.

2 Methodology and data

2.1 Identification of downhill thunderstorms

To study the downhill thunderstorms in Beijing, areas in Fig. 2a are selected as regions of interest (ROIs). Then, each ROI is divided into three subregions by terrain height: the area to the west and north of the ridge line is defined as the mountainous region (ROI_m), marked with dark gray in Fig. 2a; the area with surface elevation less than 200 m is defined as the plain region (ROI_p), marked with white; and the light-gray area between these two lines is defined as the downslope region (ROI_d).
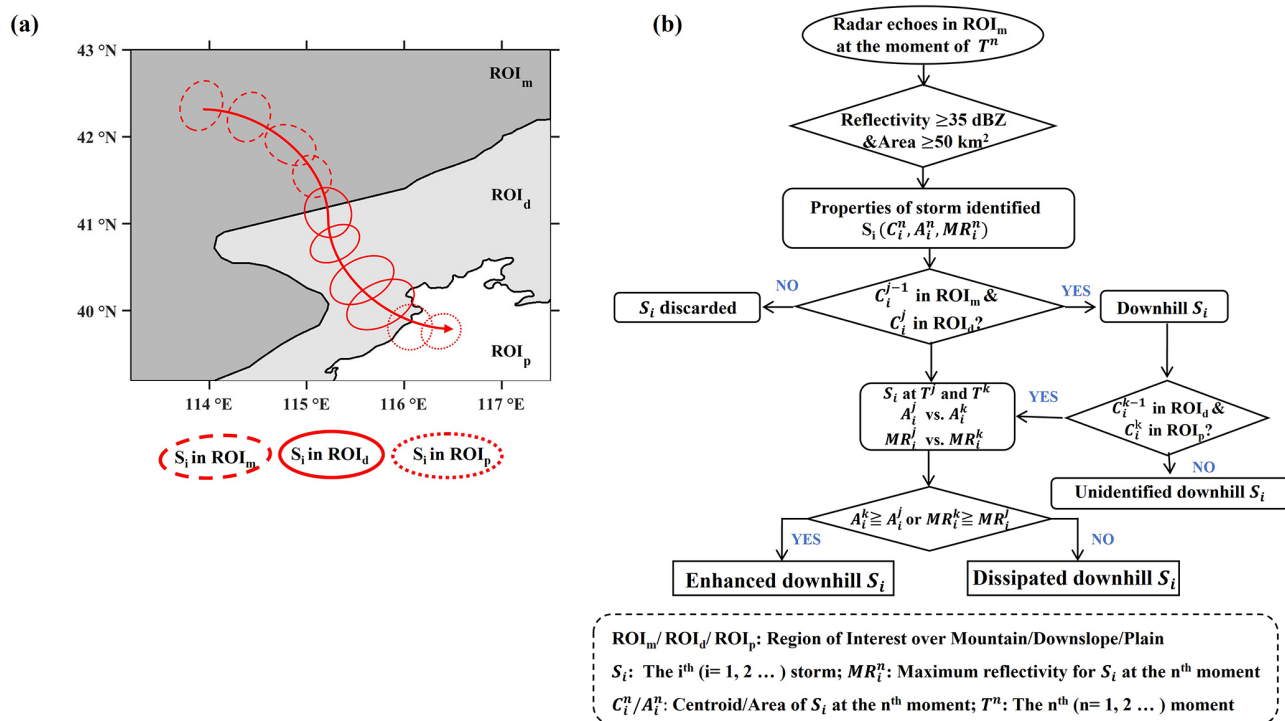
Figure 2. (a) Definition of the ROIs and the schematic diagram showing the track of a downhill thunderstorm S_i (red circle). The red arrow denotes the trajectory of S_i. **(b)** Flowchart showing the primary processes to identify downhill thunderstorms in this study.

The flowchart for identifying downhill thunderstorms from composite radar reflectivity is illustrated in Fig. 2b, which is mainly comprised of the following steps: firstly, based on the well-established findings in the literature from previous studies (e.g., Kingsmill, 1995; Weckwerth, 2000; Qin and Chen, 2017; Bai et al., 2019), echoes with radar reflectivity reaching over 35 dBZ triggered in ROI$_m$ are identify as potential downhill thunderstorms. To eliminate false signals, echoes with an area less than 50 km^2 are filtered out.

Secondly, these potential clusters are tracked using the area overlapping method (Machado et al., 1998; Huang et al., 2018; Chen et al., 2019). Noted that during merging processes, only the largest cluster is tracked continuously, while others are subsequently terminated. Likewise, during the splitting processes, only the largest cluster is tracked continuously, while others are attributed to newly initiated storms. Supposing that the ith ($i = 1, 2, \ldots$) thunderstorm (i.e., S_i) is observed in ROI$_m$ at time n (i.e., T^n), the properties of S_i^n including the centroid (C_i^n), area (A_i^n), and maximum reflectivity (MR$_i^n$) are obtained.

Thirdly, the downhill thunderstorms are defined by whether the potential clusters move into ROI$_d$ and ROI$_p$. And if the centroid of S_i crosses the ridge line and moves from ROI$_m$ to ROI$_d$ at time j, T^j is defined as the starting time when S_i begins to go down the hills. Similarly, if the centroid of S_i crosses the plain line and moves from ROI$_d$ to ROI$_p$ at time k, T^k is defined as the arrival time when S_i reaches the

plain. Then, $T^k - T^j$ is defined as the downhill duration of S_i. An example of S_i is depicted in Fig. 2a.

Finally, the downhill thunderstorms are classified into two categories: enhanced downhill storms (EDSs) and dissipated downhill storms (DDSs). These two subsets are classified by comparing the area and maximum reflectivity at time T^k to those at time T^j. If at least one of the criteria $A_i^k \geq A_i^j$ and $\text{MR}_i^k \geq \text{MR}_i^j$ is fulfilled, S_i is considered to be an EDS; otherwise, it is defined as a DDS.

Most previous research, either case studies or small-sample statistical analysis, lacks an objective criterion used to determine downhill thunderstorms. They typically focus on EDSs in the presence of high-impact weather and ignore DDSs. Compared to the existing approaches in the literature, our methodology can discriminate between these two types of downhill thunderstorms due to its capability to define the timing and location of storms and track their corresponding evolution. Therefore, this methodology can be readily applied to other regions with similar topography as long as weather radar measurements are available.

2.2 Meteorological data

As depicted in Sect. 2.1, radar reflectivity derived from the Doppler radar network dataset with a grid resolution of 0.01° at 10 min intervals during the rainy seasons (i.e., April–

Table 1. Summary of six radar wind profilers in Beijing.

Station name	Acronym	Lat. (°N)	Long. (°E)	Alt. (m a.m.s.l.)
Shangdianzi	SDZ	40.66	117.11	286.5
Huairou	HR	40.36	116.63	75.6
Yanqing	YQ	40.45	115.97	489.4
Haidian	HD	39.98	116.28	46.9
Pinggu	PG	40.17	117.12	32.1
Beijing Weather Observatory	BWO	39.79	116.47	32.5

September) in 2018–2021 is used to identify downhill thunderstorms over Beijing.

Upper-air sounding balloons launched at Zhangjiakou (ZJK) and the Beijing Weather Observatory (BWO) (see their locations in Fig. 1b) are used to provide vertical thermodynamic features during the downhill thunderstorms. Generally, the balloons are launched twice a day at 08:00 and 20:00 LST (local standard time), providing the vertical profiles of temperature, pressure, relative humidity, and horizontal winds with a vertical resolution of 5–8 m (Guo et al., 2020). For the sake of improving the prediction skill of summertime storms, an additional radiosonde launch is performed at 14:00 LST daily at the BWO for the period from 1 June to 31 August.

Ground-based meteorological variables, including 2m air temperature (T_{2m}), dew point temperature, and pressure measured at 5 min intervals, as well as precipitation measured at 1 min intervals from automated surface stations (AWSs), are also used in the analysis over the study area.

Geopotential height at 500 hPa and horizontal wind at 850 hPa from the fifth-generation ECMWF reanalysis (ERA5) datasets derived by the European Centre for Medium-Range Weather Forecasts (ECMWF) are used for analyzing the large-scale conditions in a case study of a heavy precipitation event in Beijing. The dataset has 37 pressure levels, which is made publicly accessible on a grid spacing of 0.25° at hourly intervals (Hoffmann et al., 2019).

2.3 Radar wind profiler measurements

The RWP mesonet in Beijing, as presented in Table 1 and Fig. 1b, consists of six RWPs positioned at Shangdianzi (SDZ), Huairou (HR), Yanqing (YQ), Haidian (HD), Pinggu (PG), and BWO. The RWPs used in this study are CFL-6 tropospheric wind profilers, manufactured by the 23rd Institute of the China Aerospace Science and Industry Corporation. These instruments provide sampling height, horizontal wind direction and speed, vertical wind speed, horizontal credibility, vertical credibility, and refractive index structure parameters. And the data are recorded at 6 min intervals at 34 levels with a vertical resolution of 120 m below 4 km above the ground level (a.g.l.) in low-operating mode and at 25 levels with a vertical resolution of 240 m from 4 to 10 km a.g.l. in high-operating mode (Liu et al., 2019). Considering that the

six RWPs are located at different terrain heights, the horizontal velocities measured by each RWP are interpolated to the same altitude, starting from 0.5 km above mean sea level (a.m.s.l.) with a vertical resolution of 120 m.

Dynamic parameters, such as the horizontal divergence profiles, can readily be calculated by vertical wind profile measurements derived from soundings or RWPs distributed along the perimeter of a circle or a triangle over an area (Bellamy, 1949; Carlson and Forbes, 1989; Lee et al., 1995; Bony and Stevens, 2019). The reliability of the measurements and triangle method is demonstrated in previous work (Guo et al., 2023). Thus, we also employ this methodology to calculate the regional mean divergence, vorticity, and vertical velocity profiles within the triangular regions built by the RWP mesonet.

3 A case study of an EDS event

EDSs present significant challenges for local weather forecasters in accurately predicting the intensity of precipitation during nowcasting. In this section, an observational case study of this type of downhill thunderstorm is selected to explore the role of thermodynamic and dynamic environment in the evolution of downhill thunderstorms.

This storm originated from ROI_m and began to go down the hill at 12:00 LST on 28 September 2018; it then hit Beijing after approximately 2–3 h. Several AWSs in the Yanqing District recorded lightning activity and hail accompanied by an hourly rainfall amount of over 30 mm from 14:30 to 15:30 LST. It is noteworthy that the intensity of downhill thunderstorm became weakened before 14:00 LST but intensified as it approached the plain area of Beijing.

3.1 Synoptic background

A sounding taken at ZJK (Fig. 3a) at 08:00 LST located in the westerly flow sector showed a surface-based temperature inversion below 900 hPa and a deep dry layer aloft from 850 hPa up to about 400 hPa. At the same time, similar temperature and humidity stratification was seen at the BWO (Fig. 3b) with little convective available potential energy (CAPE) of 170.8 J kg^{-1} and convective inhibition (CIN) of 61 J kg^{-1}. The veering of a northwesterly wind to a westerly

wind from 850 hPa to above 600 hPa indicated the presence of cold advection at 08:00 LST. Unfortunately, no sounding was available to elucidate the temporal evolution of atmospheric thermodynamic and dynamic environments during the passage of the EDS from 12:00 to 15:00 LST. We can only speculate that the thermal stratification seems insufficient to facilitate the initiation and subsequent organization of deep convection, even considering the possible enhancement of an unstable layer as the mixed layer grew after 08:00 LST.

Then, we resort to the synoptic pattern from ERA5 reanalysis at hourly intervals. At 500 hPa (Fig. 3c), the large-scale conditions at 14:00 LST on 28 September 2018 were characterized by a deep cold vortex at the border of Mongolia and China. Beijing was situated in the cold sector with a cold center approximately 500 km to the north and influenced by strong westerly flows. At 850 hPa (Fig. 3d), a trough extended from northeast to southwest over ROI_d, resulting in significant southwesterly flow prior to the trough over Beijing. The veering of a southwesterly wind at 850 hPa to a westerly wind 500 hPa indicated the presence of warm advection. The changeover from cold advection at 08:00 LST to warm advection at 14:00 LST in the lower troposphere could account for the subsequent deepening organization of convection after the thunderstorm entered the plain.

3.2 Radar reflectivity and surface observations

Radar reflectivity at 12:00 LST (Fig. 4a) showed that a convective line with several convective cores was detected across the ridge line and moved gradually southeastward into ROI_d driven by the low-level northwesterly flows. Surface streamlines evidently showed dominant west-to-southwesterly surface winds in ROI_m and south-to-southwesterly flows in ROI_p (also see Fig. 4a). In downslope regions, the local mountain valley orientations appeared to account for up-valley flows in various directions. A surface analysis at 12:00 LST, given in Fig. 5a, shows a humid center in the northwest of the mountain region due to the previous precipitation, whereas the relative humidity of the downslope and plain was less than 60 %. The thermal boundary near the ridge line that was generated by the terrain could also be seen. $T_{2\,m}$ over the plain area was on average greater than 20 °C, whereas the mean $T_{2\,m}$ over the mountainous region was less than 10 °C. The large northwest–southeast-oriented temperature gradient appeared to account for the intensification and better organization of the EDS at 12:30 LST (Fig. 5b). Surface convergence emerged ahead of the convective line, indicated by the streamlines in Fig. 4b, which were associated with a pre-squall mesotrough and mesolow.

At 13:00 LST, the convective line with reflectivity exceeding 35 dBZ had split into two segments (Fig. 4c). The northern segment was completely separated from the main storm in the southwest and then expanded northeastward by the intersecting streamlines, with another convective cell initiated

near the local converging center around 41.5° N, 117° E before 13:30 LST (Fig. 4d). The southern segment was maintained with the total rainfall exceeding 10 mm from 13:00 to 14:00 LST. Meanwhile, the wet center gradually moved eastward to the northeast of the mountain region (Fig. 5c and d). Until 14:00 LST, the convective cells started to merge into a linear convective system, and the frontal edge of the convection line had arrived at triangle 1 with weaker intensity than before (Fig. 4e).

Further, we attempt to examine the roles of the cold pool and low-level wind shear in maintaining the intense squall line in accordance with the theory of Rotunno et al. (1988). However, it is difficult to perform a comprehensive and quantitative analysis due to the inhomogeneous environment and measurement. Here, we qualitatively use the horizontal winds over YQ (Fig. 6a) to estimate vertical wind shear (VWS) on the downslope and $T_{2\,m}$ to identify a cold pool (Fig. 5). At 13:00 LST, the wind speed below 1.5 km a.m.s.l. was weaker than 5 m s^{-1}, while it was stronger than 15 m s^{-1} above 2.5 km a.m.s.l. The maximum value of VWS occurred at the altitude of 1.8 km a.m.s.l. with the value exceeding 20 m s^{-1} km^{-1}. In less than 10 min, cold downdrafts produced a sharp drop in $T_{2\,m}$ by 6 °C in the south of the convective cells (Fig. 5c and d). The effects of the resulting low-level VWS might balance those of the cool pool, which helped stimulate the development of more intense storms from 13:00 to 13:30 LST. Meanwhile, the accompanying evaporative cooling in the descending flows strengthened the cold pool. After 13:30 LST, horizontal wind speeds in the lowest 2 km layer strengthened to shrink the low-level VWS to about 10 m s^{-1} km^{-1}. The cold-pool-induced horizontal vorticity could overpower that of the low-level wind shear, partly facilitating the dissipated radar echo before 14:00 LST (Fig. 5e). Moreover, this might be related to the relatively strong cold pool located in the south, which potentially cut off the warm southerly inflow from the plains to the mountains. Then, the cool pool weakened with convection and the overpowering effect diminished.

As the storm approached ROI_p from 14:00 LST, composite radar reflectivity shows that it was significantly strengthened to an intense and well-organized squall line (Fig. 4e–g). AWSs within triangle 1 captured its associated rainfall. An abrupt increase in surface pressure by +3 hPa was seen across the gust front in triangle 1 when the maximum rainfall rate exceeded 3 mm (6 min)$^{-1}$ (not shown). Except for the abovementioned balanced state between the cool pool and low-level vertical wind shear, this enhancement could potentially be associated with the dynamic lifting over the plain area. Due to the disadvantage of surface observations in monitoring the vertical dynamic features, we have to resort to the examination of the evolution of high-resolution divergence and vertical velocity derived from the fine-scale RWP mesonet in the following subsection.
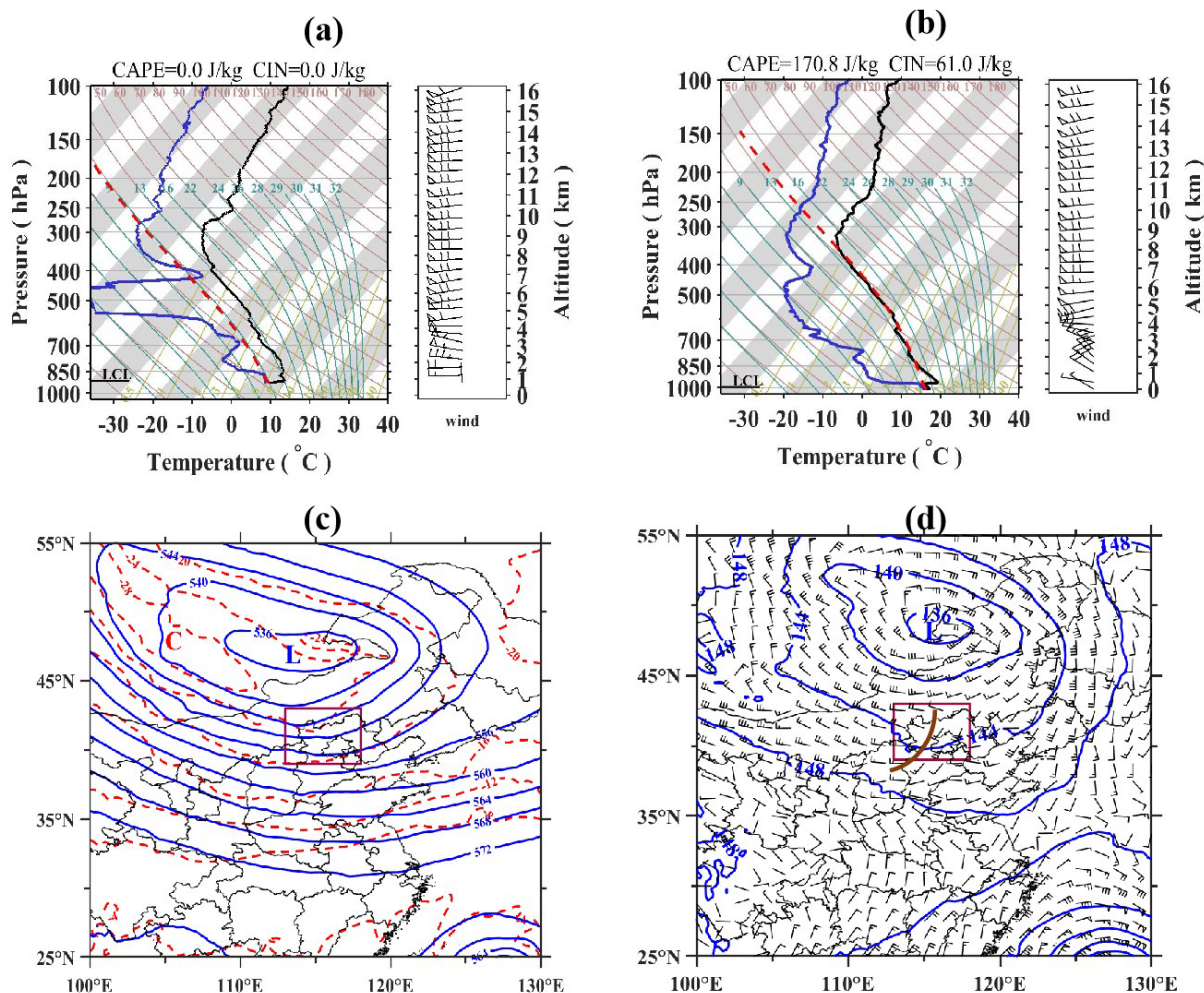
Figure 3. (a) SkewT and log P diagram derived from the upper-air sounding at ZJK at 08:00 LST on 28 September 2018. **(b)** Same as **(a)** but for the upper-air sounding at the BWO. **(c)** Horizontal distribution of geopotential height at 500 hPa (solid blue lines at 40 gpm intervals) and temperature at 500 hPa (dashed red lines at intervals of 4 °C) at 14:00 LST on 28 September 2018, both of which are obtained from the ERA5 hourly reanalysis data. The purple rectangle indicates the location of the study area shown in Fig. 1b. The letters "L" and "C" denote the centers of a low-pressure system and cold air, respectively. **(d)** Same as **(c)**, but for the fields of geopotential height at 850 hPa (solid blue lines at 40 gpm intervals) and horizontal wind at 850 hPa. Note the distribution of a trough along the thick brown line.

3.3 Divergence and vertical velocity

Before the convective system reached the plain area, sustained southwesterly wind above 2 km a.m.s.l. was observed after 12:00 LST at YQ (Fig. 6a), which was likely driven by the synoptic pattern, accompanied by upper-layer divergence and downdraft in triangle 1 (Fig. 6b). The much weaker near-surface southerly wind and unnoticeable divergence could to a certain extent be influenced by the valley flows at the foot of the mountains. Meanwhile, a peak of positive vorticity exceeding $10^{-4}\,\mathrm{s}^{-1}$ and a deep layer of negative vorticity up to 5 km a.m.s.l. in triangle 1 were maintained during this time period (Fig. 6c). Then, pronounced southerly wind occurred after 13:00 LST that corresponded to the rapid intensification in convergence below 2 km, providing an uplifting back-

ground, albeit less than $0.1\,\mathrm{m\,s}^{-1}$. This updraft assisted the upward transport of moist air in the planetary boundary layer (PBL), which facilitated the subsequent formation of clouds and convective rainfall. Additionally, a vorticity maximum near $3 \times 10^{-4}\,\mathrm{s}^{-1}$ at 13:48 LST in the PBL might also be favorable for organized convective development.

The low-level wind speeds over YQ started to increase to $10\,\mathrm{m\,s}^{-1}$ as a result of the downward momentum transport. The subsequent enhancement in convergence coincided well with the intensification of southwesterly winds ($> 10\,\mathrm{m\,s}^{-1}$) up to 3 km a.s.m.l. after 14:18 LST. Such intensification in convergence and updraft were also well captured by triangle 2 (not shown), even with more than 1 h in advance of the convective rainfall arrival. Upward motion in triangle 1 increased in amplitude and deepened rapidly in depth as the
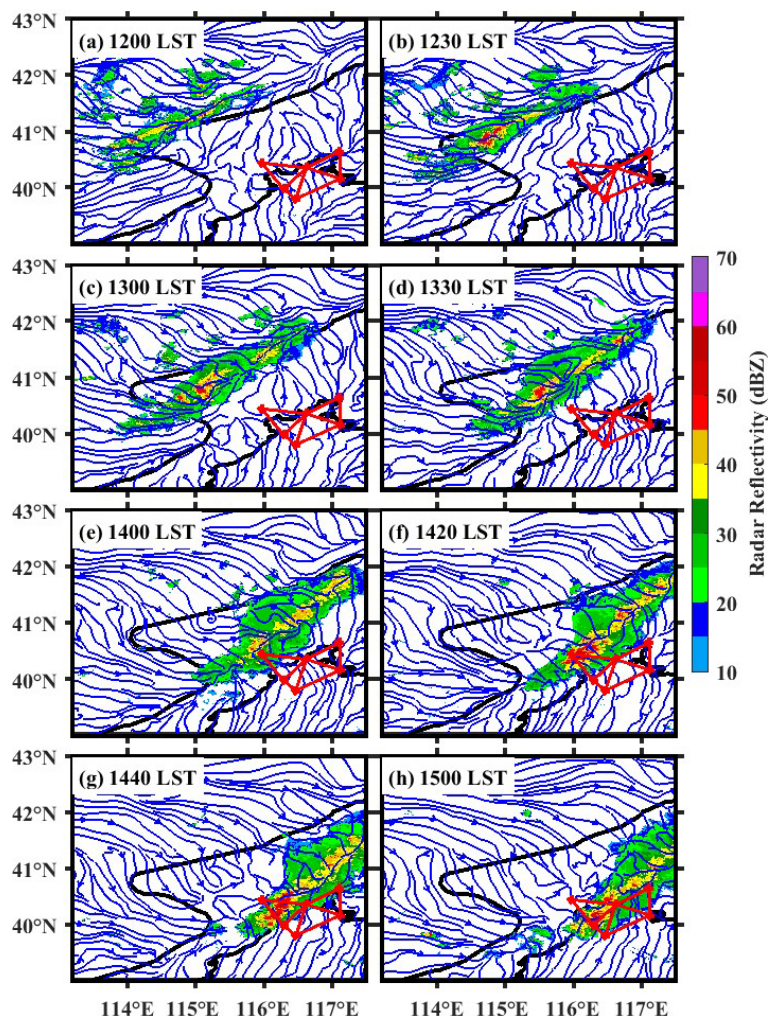
Figure 4. Evolution of the composite radar reflectivity (color-shaded, dBZ) and surface streamlines derived from AWSs for the case of an EDS event occurring during the period from **(a)** 12:00 to **(h)** 15:00 LST on 28 September 2018. The four red triangles denote the regions used to calculate the horizontal divergence and vertical motion with the triangle method.

squall line propagated southeastward and triggered rainfall over triangle 1. The most intense convergence occurred at 14:30 LST and extended from 1 km to above 2.5 km a.m.s.l. afterwards as a result of latent heat release during cloud formation. The maximum vertical velocity reached $0.35 \, \mathrm{m \, s^{-1}}$ around 3.5 km a.m.s.l., which was about 6 min prior to the peak area-averaged rainfall rate at 14:48 LST. The significant convergence diminished after 14:54 LST, when deep convection moved out of triangle 1 (Fig. 4h). Downdrafts are found with moderate upward and downward motions in the stratiform area.

Interestingly, as the squall line propagated eastward and approached the urban center after 15:00 LST, it rapidly dissipated as the area of convective echo was reduced by 80 % until 16:00 LST (not shown). This appeared to result from the blocking of the water supply by the high-rises over Beijing's built-up area, the so-called "urban bifurcation" effects

on moving thunderstorms (Changnon, 1981; Zhang, 2020). In this case, deep convection in the urban center and northern suburban area was suppressed due to the urban blocking effects. It was consistent with the persistent low-level divergence over triangles 3 and 4 with a maximum value of $3 \times 10^{-4} \, \mathrm{s^{-1}}$ occurring near the surface (not shown). Clearly, this result can help us understand the urban building-barrier-induced divergence and the dissipation of thunderstorms.

4   Comparison with a DDS event

In the preceding section, low-level convergence is an effective signal for the maintenance of an EDS event. In this section, we present a DDS event that occurred on 23 June 2018 in an attempt to investigate the difference in the pre-storm environment for two types of downhill thunderstorms. Similar to the trajectory of the EDS, the DDS began to go downhill at
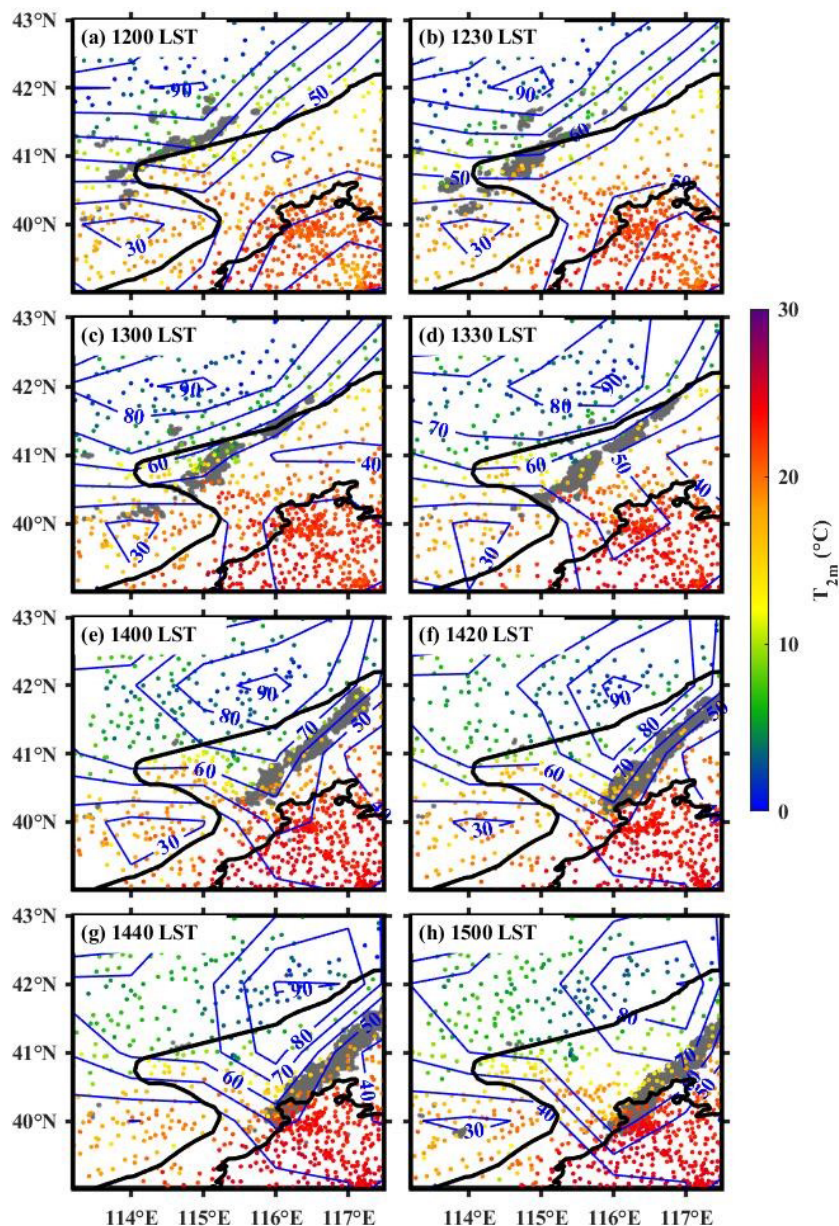
Figure 5. Evolution of the $T_{2\,m}$ (color-shaded, °C) and relative humidity (contour, %) derived from AWSs from **(a)** 12:00 to **(h)** 15:00 LST on 28 September 2018. The gray region denotes the position of echo with radar reflectivity exceeding 35 dBZ.

16:00 LST (Fig. 7a) and then propagated southeastward with an area larger than 1000 km^2. It had dissipated rapidly upon reaching the plain of Beijing after 19:00 LST and diminished until 21:00 LST.

Figure 8a shows the skewT–log P diagram derived from the sounding taken at the BWO at 14:00 LST on 23 June 2018. It can be seen that a dry troposphere was presented in the early afternoon. As time lapsed, the humidity above 700 hPa increased at 20:00 LST (Fig. 8b), even though the surface was characterized by a dry layer near the surface. The surface relative humidity was less than 40 % with $T_{2\,m}$ ex-

ceeding 30 °C and the dew point temperature less than 20 °C. The CIN slightly decreased from 280.2 J kg^{-1} at 14:00 LST to 264.0 J kg^{-1} at 20:00 LST. By comparison, The CAPE increased from 35.5 J kg^{-1} at 14:00 LST to 483.0 J kg^{-1} at 20:00 LST. As shown in Fig. 8c, the study area was situated to the west of the high-pressure ridge at 500 hPa and influenced by northerly flows in front of the ridge, whereas the lower levels were dominated by weak southwesterly winds below 850 hPa.

In the next section, we examine the dissipation stage of a downhill storm when it reached triangle 1 with a focus
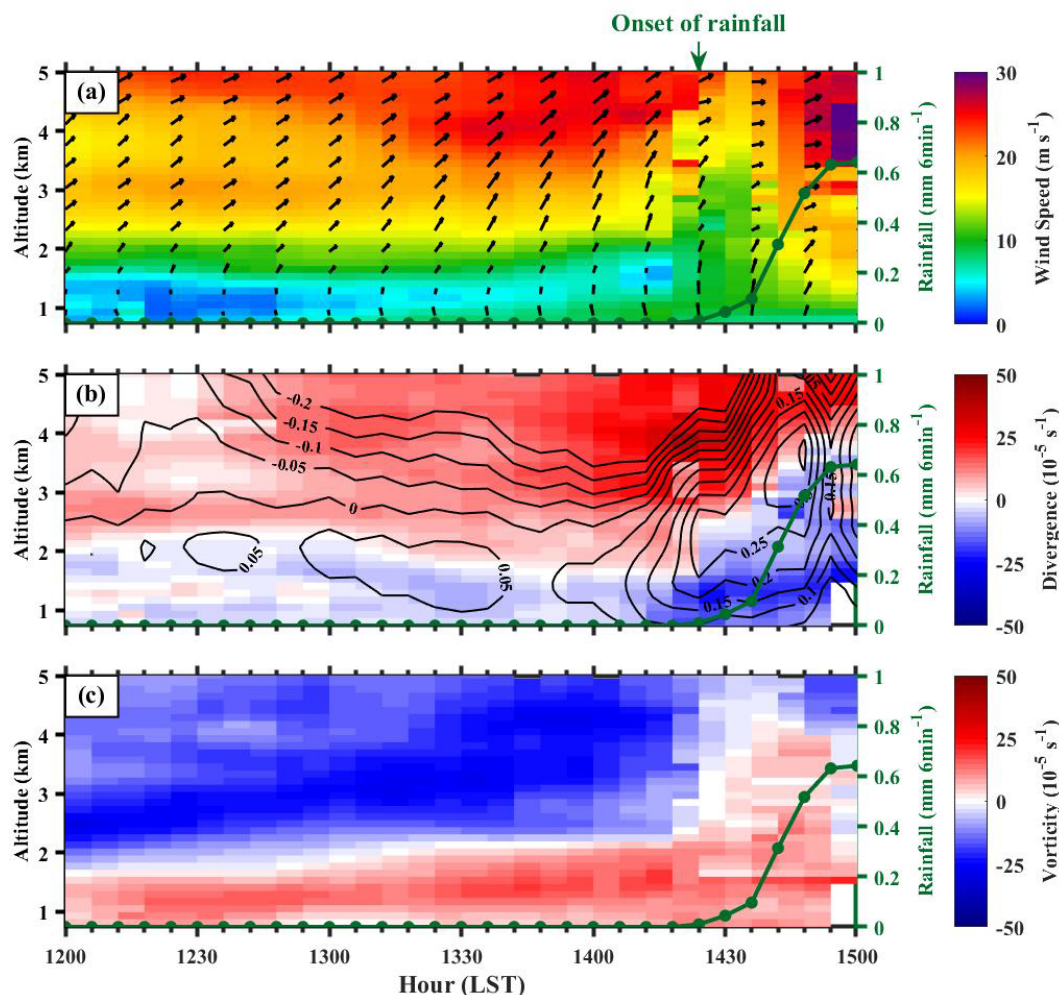
Figure 6. (a) Time series of horizontal wind vectors ($\mathrm{m\,s^{-1}}$) with wind speeds shaded in the 0.5–5 km a.m.s.l. layer during the period of 12:00–15:00 LST on 28 September 2018 at YQ station. Green dotted lines represent the triangle-area-averaged rainfall amount ($\mathrm{mm\,6\,min^{-1}}$) of triangle 1. **(b)** Same as **(a)**, but for the vertical profiles of the triangle-averaged divergence (shaded, $10^{-5}\,\mathrm{s^{-1}}$) and vertical velocity (contour, $\mathrm{m\,s^{-1}}$) for triangle 1. **(c)** Same as **(b)**, but for the vertical profiles of the vorticity (shaded, $10^{-5}\,\mathrm{s^{-1}}$) for triangle 1.

on the evolution of atmospheric dynamic variables. A sustained near-surface southeasterly wind was found over YQ before 19:00 LST from the surface streamlines and vertical wind profile that are shown in Figs. 7b–c and 9a. The low-level troposphere over triangle 1 was dominated by distinct deep divergence (Fig. 9a) and positive vorticity (Fig. 9b) below 2 km a.m.s.l. The deep divergence of regional flows and larger CIN more tended to suppress the vertical motion breaking through the resistance of a stable atmosphere (Xiao et al., 2019).

As the downhill thunderstorm reached YQ at 19:00 LST (Fig. 7d), the near-surface wind turned into weak northwesterly winds accompanied by the rapid intensification of convergence over triangle 1 under the force of the convective system itself. The strongest convergence of this event with a value of $-3.8 \times 10^{-4}\,\mathrm{s^{-1}}$ below 1 km a.m.s.l. occurred at 19:06 LST. It is worth noting that the divergence layer above

1.5 km a.m.s.l. persisted during the occurrence of precipitation after 19:24 LST. Even though there were cyclone motions and weak updrafts with the maximum vertical velocity reaching $0.1\,\mathrm{m\,s^{-1}}$, it was not enough to penetrate the divergence layer and lift the vapor to the lifting condensation level (LCL) at around 800 hPa as shown in Fig. 8b. The maximum composite radar reflectivity of the echo sharply decreased from 64.5 dBZ at 19:00 LST to 53.5 dBZ at 20:00 LST with the area shrinking by half (Fig. 7e). The rainfall was terminated, which was consistent with the dominant low-level divergence until 21:00 LST (Fig. 7f).

The above comparison indicates that a linear system was intensified into the squall line with fast speed in front of a shortwave trough in the EDS event. In the DDS event, some scattered convective cells were organized into clusters as they propagated to the plain under a weak ridge and then dissipated. For these two cases for the EDS and DDS events,
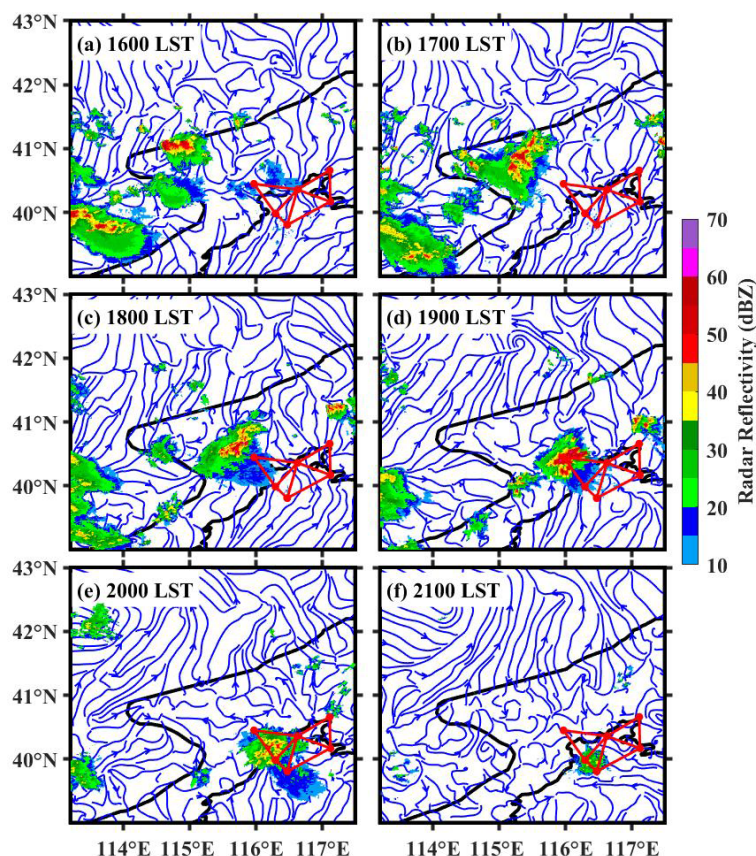
Figure 7. Same as Fig. 4, but for the case of a DDS event occurring during the period from **(a)** 16:00 to **(f)** 21:00 LST on 23 June 2018.

the thermal stratification indicated the presence of unfavorable pre-storm environmental settings with insufficient unstable energy and inadequate moisture. The dynamic condition played a pivotal role for convective development during the passage of the downhill thunderstorm. Compared with the DDS event, the enhanced southerly winds and corresponding convergence in the lower level were distinct features of the EDS. The above results indicate that the RWP mesonet could capture the vertical profiles of horizontal divergence and vertical motion well, favorably supporting the detection of convection.

Notably, small-scale variations of airflow in the narrow valley at the intersection of Mt. Taihang and Mt. Yan undoubtedly impact the dynamics of the EDS and DDS events (Xiao et al., 2017). In other words, the storms from the northwest need to pass by the downslope, valley, and then upslope to reach the plain. The complex local terrain should be taken into account as factors for the evolution of thunderstorms during the southeastward propagation. However, the current resolution of observations is not capable of resolving the dynamic processes associated with the convective development in that region. We hope to further explore this factor with the help of numerical simulations in the future.

5 Statistical results

5.1 General features of downhill thunderstorm events

To obtain a more robust understanding of the climatology for downhill thunderstorm evolution in Beijing, an in-depth statistical analysis is carried out in this study. According to the methodology mentioned in Sect. 2.1, we firstly identify a total of 95 downhill thunderstorms triggered in ROI_m that moved into ROI_d and ROI_p in the study area (Fig. 1b) based on the radar reflectivity datasets during the rainy seasons (i.e., April–September) in 2018–2021. We perform a statistical analysis of the occurrence number of radar reflectivity that is equal to or greater than 35 dBZ on a grid spacing of 0.01° at 10 min intervals during these downhill thunderstorm events.

As shown in Fig. 10a, downhill thunderstorms tend to initiate in ROI_d with strong steep slopes near the ridges of the Yan Mountains associated with solar heating in the afternoon. The highest-frequency center is found mainly over the western downhill area extending to the plain with the occurrence number exceeding 400, possibly due to the large amount of eastward propagation of thunderstorms driven by the westerly or southwesterly flows during the warm seasons in Beijing (Chen et al., 2012, 2014).
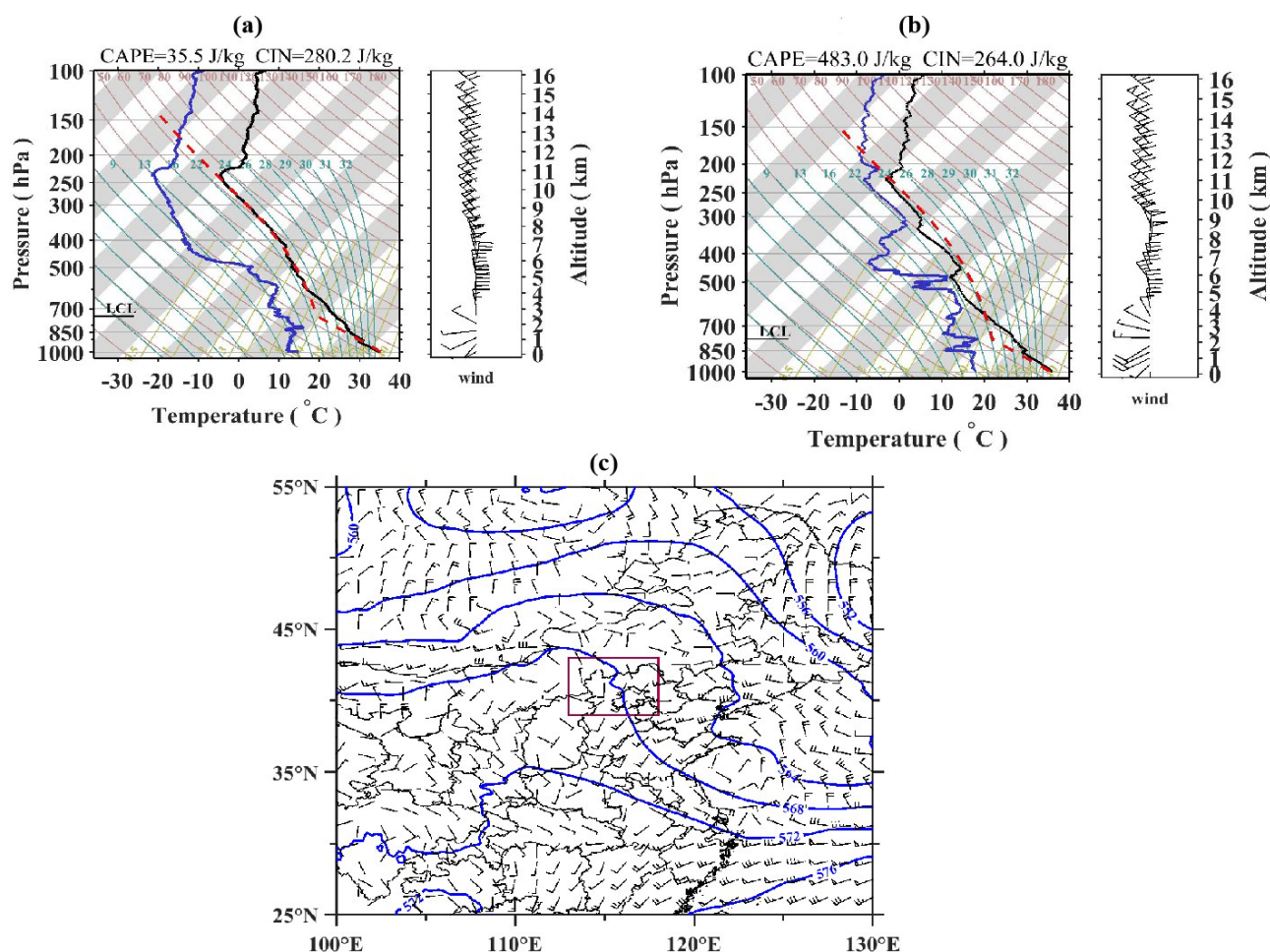
Figure 8. SkewT and log P diagram derived from the upper-air sounding at the BWO at **(a)** 14:00 LST and **(b)** 20:00 LST on 23 June 2018. **(c)** Horizontal distribution of geopotential height at 500 hPa (solid blue lines at 40 gpm intervals) and horizontal winds at 850 hPa (wind barbs) at 20:00 LST on 23 June 2018, which are both obtained from the ERA5 hourly reanalysis data. The purple rectangle indicates the location of the study area shown in Fig. 1b.

For all downhill thunderstorms, the relationship of the initial area and length to width ratio of thunderstorms at the beginning and the relative variation of area to the time it arrives at ROI_p is analyzed. Here, we record the maximum (minimum) axis length of the radar echo with reflectivity ≥ 35 dBZ as the length (width) of the downhill thunderstorm. The area and length to width ratio tend to reflect the horizontal scale and organization of convective storms. Generally, linear convective storms show a length to width ratio greater than or equal to 3.0 (Chen and Chou, 1993; Meng et al., 2013; Yang et al., 2017). The results show that several mature thunderstorms with an area larger than 5000 km^2 tend to dissipate during the downhill process with weaker intensity and area, which is likely due to the splitting processes (Fig. 10b). Convective lines commonly intensify to squall lines, but several isolated and loose thunderstorms expand rapidly during the downhill process with increasing area when entering the

plain, which may be associated with the favorable regional-scale lower tropospheric environment.

It is found that 63 thunderstorm events tended to be enhanced after moving into the downhill and urban areas, accounting for about 66 % of the total number of downhill thunderstorm events, whereas 32 thunderstorm events tended to be dissipated. Most of the DDSs arrive at the plain area in mornings and late afternoons (Fig. 10c). Specifically, 11 and 18 DDSs arrive at the plain area during the period of 06:00–12:00 and 16:00–00:00 LST, which account for 34 % and 56 % of all DDSs, respectively. In contrast, the EDSs tend to occur in early mornings and afternoons. A total of 18 and 43 EDSs arrive at the plain area before 08:00 LST and after 14:00 LST, respectively, corresponding to percentages of 26 % and 68 %. Mesoscale circulations driven by the urban heat island (UHI) effect and topography may contribute to the difference of downhill storm durations. As presented by Dou et al. (2015), the magnitude of the UHI in Beijing
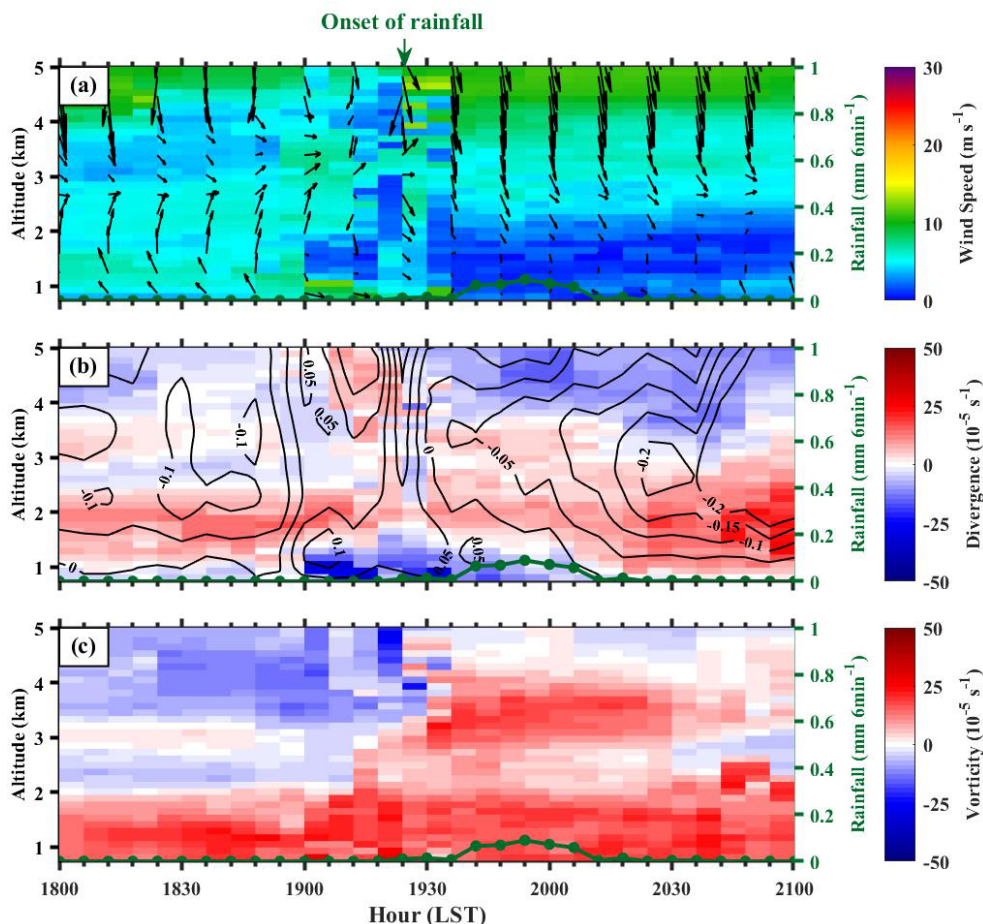
Figure 9. (a) Time series of horizontal wind vectors ($m\,s^{-1}$) with wind speeds shaded in the 0.5–5 km a.m.s.l. layer during the period of 18:00–21:00 LST on 23 June 2018 at YQ station. Green dotted lines represent the triangle-area-averaged rainfall amount ($mm\,6\,min^{-1}$) of triangle 1. **(b)** Same as **(a)**, but for the vertical profiles of the triangle-averaged divergence (shaded, $10^{-5}\,s^{-1}$) and vertical velocity (contour, $m\,s^{-1}$) for triangle 1. **(c)** Same as **(b)**, but for the vertical profiles of the vorticity (shaded, $10^{-5}\,s^{-1}$) for triangle 1.

at nighttime is stronger than in daytime. In the early morning, low-level westerly and northwesterly winds converged into the Beijing's plain area because of a combination of downslope mountain breezes and strong-UHI-induced convergence, which accelerate the speed of thunderstorms towards the plain. The weaker southeasterly upslope valley breezes in the late afternoon and evening make downhill storms slow down and contribute to the prolonged duration. One caveat is that the conclusions may vary by the number of available sample cases.

5.2 Dynamic conditions

Figure 11 presents the spatial distributions of trajectories for the two types of downhill storm events according to the methodology described in Sect. 2.1. Limited by the number of samples, the moving directions are not categorized. However, it is obvious that the eastward and southeastward trajectories are dominant rather than the southward and southwest-

ward ones. This distinct feature confirms that the western part of ROI_d is a key area for the development of downhill thunderstorms. To better understand the similarities and differences between EDS and DDS from the perspective of the ambient atmospheric environment, three-dimensional dynamic structures derived from the RWP mesonet are analyzed. Variables including wind speed, vertical wind shear, u component and v component of wind, divergence, and vorticity profiles are used to provide information on dynamic structures before the downhill thunderstorms arrive. Thus, we select 68 downhill thunderstorms, including 50 EDSs and 18 DDSs, which pass through triangle 1 to the plain among all 95 samples and focus on these mesoscale parameters from YQ station and triangle 1 in the following discussions.

The mean vertical wind profiles 2 h prior to the arrival of the thunderstorms are investigated. Horizontal wind speed, vertical wind shear, u component, and v component from the RWP in YQ, as well as divergence and vorticity over triangle 1, are calculated (Fig. 12). Results indicate that wind
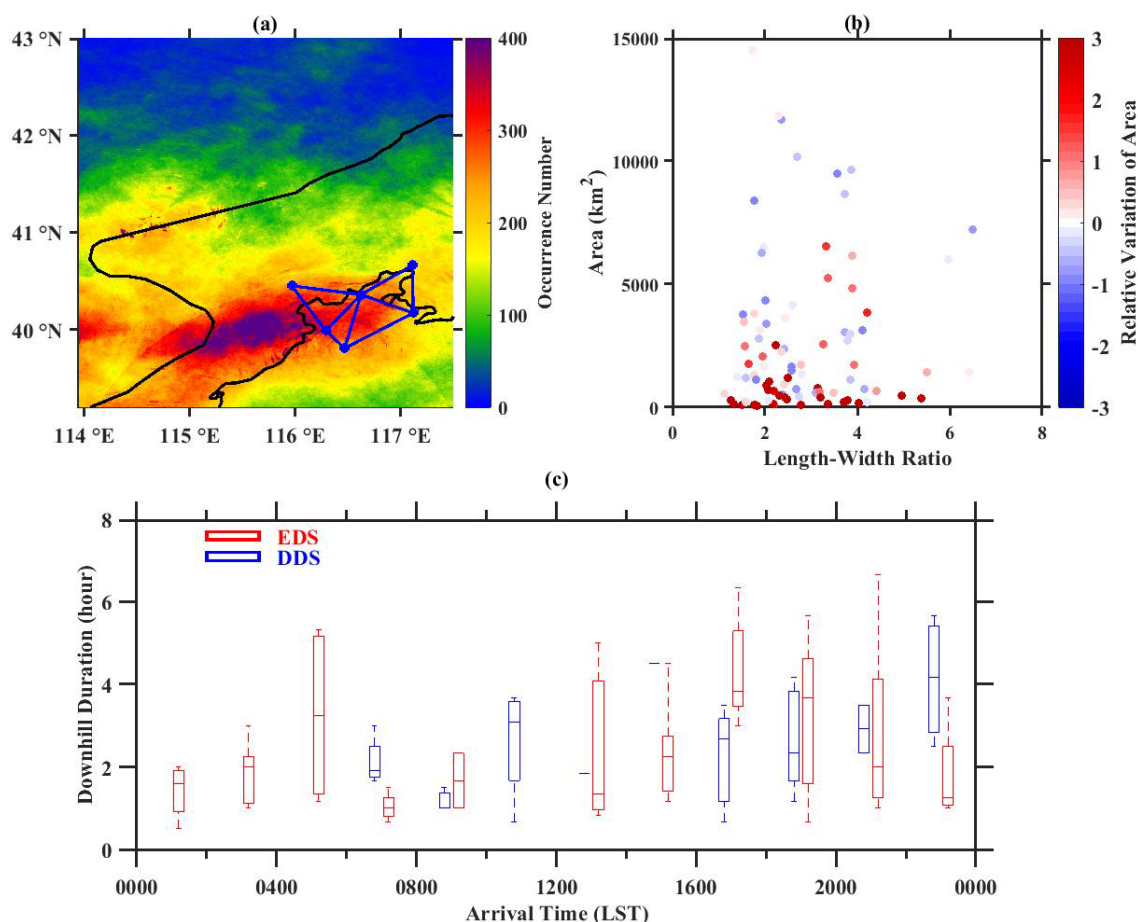
Figure 10. (a) The occurrence number (shaded) of reflectivity greater than 35 dBZ during downhill thunderstorm events. **(b)** Scatterplots showing the distribution of the initial length to width ratio and area of downhill thunderstorms, with the corresponding relative variation of area (shaded, km^2). **(c)** Box plots showing the distribution of the arrival time and downhill duration of EDSs (red) and DDSs (blue). The central box represents the values from the lower to upper quartile (25th–75th percentile); the vertical line extends from the 10th to 90th percentile, and the solid line denotes the median.
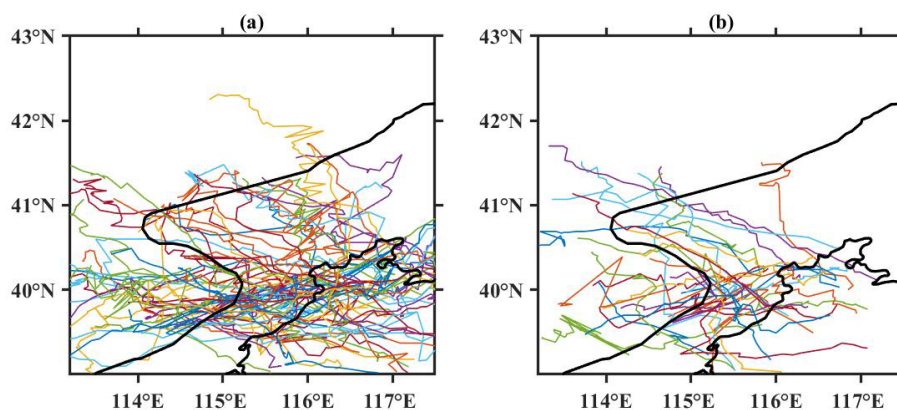
Figure 11. The spatial distribution of the trajectories (color-shaded curves) of **(a)** 63 enhanced downhill storms (EDSs) and **(b)** 32 dissipated downhill storms (DDSs) as detected by the methodology in Sect. 2.1.

speed preceding EDSs and DDSs is about $5\,\mathrm{m\,s^{-1}}$ below 1.5 km (Fig. 12a). Much stronger horizontal winds with a maximum wind speed exceeding $15\,\mathrm{m\,s^{-1}}$ are observed in the 1.5–5 km layer in advance of the EDS events. The VWS below 5 km a.m.s.l. has no significant differences between EDSs and DDSs before their arrival (Fig. 12b). But the VWS preceding EDS events is little bit stronger than that preceding DDS events, which could likely be associated with the critical influence that high vertical wind shear exerts on convection. EDSs and DDSs mainly appear under the near-surface southeasterly and prevalent southwesterly low-level flow near the foothills. The persistent supply of water vapor is key for the successful propagation to the plains of downhill storms but does not determine the enhancement or dissipation of convection. Notably, the average v component of the wind decreases to near-zero above 3 km a.m.s.l. The existence of stronger westerly flow above 3 km a.m.s.l. is a favorable condition for the intensification of downhill storms (Fig. 12c), which corroborates the results from the case study well.

The mean vertical structure of divergence and vorticity is given in Fig. 12e and f. Before the arrival of downhill storms, one can see the presence of weak divergence near the surface due to the weak wind. Compared with EDSs, the divergence around 1.5–3 km a.m.s.l. is more evident near the arrival of DDSs with a maximum value of $10^{-4}\,\mathrm{s^{-1}}$. When thunderstorms pass by, the strong divergence in the low level is not conducive to the extension of upward movement within the boundary layer, which is attributed to the dissipation of storms, especially when instability and moisture supply are unfavorable. In contrast, the high-level divergence at altitudes of around 4–5 km promotes the compensation of the moist air and the upward transport of heat, which ultimately intensify the storm. The vorticity field in Fig. 8f is characterized by cyclonic flows at lower levels and anticyclonic flows at midlevel, which is possibly dependent on the synoptic forcing. The vorticity prior to EDSs seems to be stronger than that of DDSs, and the cooperation between lower-level cyclones and less divergence of convective system tends to promote the maintenance of updrafts, leading to heavy rainfall.

In previous work, it has been confirmed that these dynamical variables derived from the RWP mesonet in Beijing provide strong support for machine-learning-based prediction of severe convection (Wu et al., 2023). The results therein show that the usage of RWP observational data as the random forest model input tends to result in better performance in the rainfall and non-rainfall forecast 30 min in advance of rainfall onset than using the ERA5 reanalysis data as inputs. In the future, these dynamic observations and methodologies need to be further incorporated into machine learning models for improving the prediction skill of downhill thunderstorms.
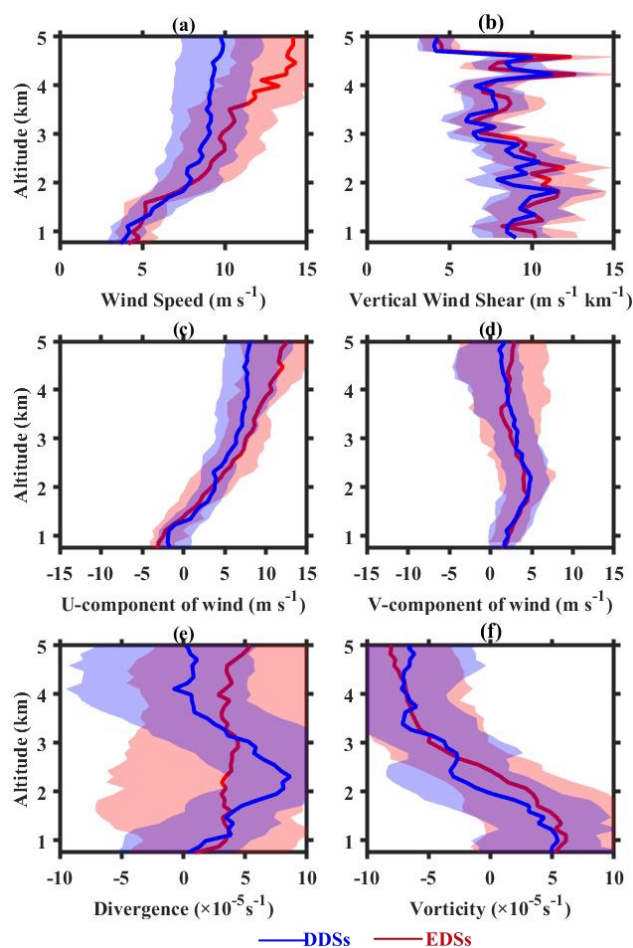
Figure 12. Vertical profiles of **(a)** wind speed, **(b)** vertical wind shear, **(c)** u component of wind, and **(d)** v component of wind over YQ station in the 2 h prior to the arrival of EDSs (red) and DDSs (blue). Panels **(e)** and **(f)** are the same as the above, except for the divergence and vorticity over triangle 1 as shown in Fig. 1b, respectively.

6 Summary and concluding remarks

Given the large uncertainty in prediction and huge impact, here we revisit the evolution of downhill thunderstorms and concurrent ambient atmospheric dynamic structures as derived from a high-density radar wind profiler (RWP) mesonet in Beijing. This RWP mesonet in Beijing is shown to be capable of continuously observing the horizontal wind fields in the lower troposphere with ultrahigh vertical and temporal resolutions. It follows that the profiles of vertical wind shear, divergence, and vorticity are derived from the triangle algorithm, which are used to analyze the pre-storm dynamic environment for the downhill storms.

First of all, a novel objective methodology has been developed to identify and track the downhill thunderstorms. Combined with the changes in area or intensity of radar echoes, enhanced downhill thunderstorms (EDSs) and dis-

sipated downhill thunderstorms (DDSs) are discriminated. A case study of an EDS during the time period of 12:00–15:00 LST on 28 September 2018 is performed. Of interest is that the intensity of the linear convective system became weaker before 14:00 LST but intensified as it approached the plain area of Beijing. Meanwhile, we present a DDS event that occurred on 23 June 2018 in an attempt to investigate the difference in the pre-storm environment for two types of downhill thunderstorms. The observational analysis of the ECMWF reanalysis, upper-air soundings, and AWSs data showed the presence of thermal conditions with insufficient unstable energy and inadequate moisture. For the case of EDS, the dynamic structures may exert a critical influence on the development of storms including strong vertical wind shear and enhanced southerly winds with corresponding convergence near the foothills. This intense convergence was also possibly associated with the outflow of a convectively generated cold pool by the squall line. By comparison, the sustained low-level divergence during the DDS event suppressed the extension of updrafts within the boundary layer, which was unfavorable for the development of organized convection.

To obtain a robust result concerning the evolution characteristics of downhill thunderstorms in Beijing, an in-depth statistical analysis is merited. The beginning and arrival time of a downhill thunderstorm event are defined as the moment when the centroid crosses the ridge line and plain, respectively. A total of 95 downhill thunderstorm events occurring in the study area are identified based on the datasets of radar reflectivity at 10 min intervals during the rainy seasons (i.e., April–September) of 2018–2021. Statistical analysis suggests that 63 thunderstorms tend to be enhanced with larger area or radar reflectivity after moving into the downhill and urban areas, accounting for about 66 %. This indicates that most of the downhill thunderstorms occur in the plains in the morning and late afternoon. Moreover, the high-occurrence-frequency center of convection is found to mainly reside west of Beijing's plain area, and the area variation of convection is not sensitive to the initial morphology itself.

Thus, we illustrate the statistical analysis of dynamic quantities, such as horizontal winds, vertical wind shears derived from the RWP at the mountain foot, and divergence and vorticity derived from the westernmost triangular region in the RWP mesonet, in relation to the enhanced and dissipated downhill storms. Results indicate that the near-surface southeasterly and low-level southwesterly flows near the foothills are conducive to successful propagation to the plains of downhill storms. Weaker lower-level divergence over the plain, along with cyclones, contributes to the development of robust updrafts and closer coupling between the boundary layer and clouds, which favors the intensification of downhill thunderstorms. Furthermore, the compensation for deepening the upward movement is aided by much stronger westerly winds and divergence observed at higher altitudes in advance of the EDS events.

Fine-scale profiling of accurate dynamic quantities will make it possible to enable a more critical and quantitative evaluation for the development of downhill thunderstorms in the future. Nevertheless, the abovementioned dynamic features, which are necessary to diagnose the evolution of thunderstorms, are not adequate to fully characterize the environment in which downhill storms are embedded. In particular, more explicit analysis of thermodynamic parameters, such as the CAPE, K index, and precipitable water, are warranted to better characterize the pre-storm environments in detail.

Author contributions. The study was completed with close cooperation between all authors. JG designed the research framework. XG and JG performed the analysis and drafted the original manuscript. JG, TC, NL, FZ, and YS helped revise the manuscript.

References

Bai, L., Meng, Z., Huang, Y., Zhang, Y., Niu, S., and Su, T.: Convection initiation resulting from the interaction between a quasi – stationary dryline and intersecting gust fronts:

A case study, J. Geophys. Res.-Atmos., 124, 2379–2396, https://doi.org/10.1029/2018JD029832, 2019.

Bellamy, J. C.: Objective calculations of divergence, vertical velocity and vorticity, B. Am. Meteorol. Soc., 30, 45–49, https://doi.org/10.1175/1520-0477-30.2.45, 1949.

Bony, S. and Stevens, B.: Measuring area-averaged vertical motions with dropsondes, J. Atmos. Sci., 76, 767–783, https://doi.org/10.1175/JAS-D-18-0141.1, 2019. .

Carlson, C. A. and Forbes, G. S.: A case study using kinematic quantities derived from a triangle of VHF Doppler Wind Profilers, J. Atmos. Ocean. Tech., 6, 769–778, https://doi.org/10.1175/1520-0426(1989)006<0769:ACSUKQ>2.0.CO;2, 1989.

Castro, A., Sánchez, J. L., and Fraile, R.: Statistical comparison of the properties of thunderstorms in different areas around the Ebro-Valley (Spain), Atmos. Res., 28, 237–257, https://doi.org/10.1016/0169-8095(92)90011-x, 1992.

Changnon, S. A.: METROMEX: a review and summary, Meteor. Mon., 40, 181, https://doi.org/10.1007/978-1-935704-29-4, 1981.

Chen, D., Guo, J., Yao, D., Lin, Y., Zhao, C., Min, M., Xu, H., Liu, L., Huang, X., Chen, T., and Zhai, P.: Mesoscale convective systems in the Asian monsoon region from Advanced Himawari Imager: Algorithms and preliminary results, J. Geophys. Res.-Atmos., 124, 2210–2234, https://doi.org/10.1029/2018JD029707, 2019.

Chen, G. T. J. and Chou, H. C.: General characteristics of squall lines observed in TAMEX, Mon. Weather Rev., 121, 726–733, 1993.

Chen, M., Wang, Y., Gao, F., and Xiao, X.: Diurnal variations in convective storm activity over contiguous North China during the warm season based on radar mosaic climatology, J. Geophys. Res.-Atmos., 117, D20115, https://doi.org/10.1029/2012JD018158, 2012.

Chen, M., Wang, Y., Gao, F., and Xiao, X.: Diurnal evolution and distribution of warm - season convective storms in different prevailing wind regimes over contiguous North China, J. Geophys. Res.-Atmos., 119, 2742–2763, 2014.

Chen, M., Xiao, X., and Gao, F.: Dynamical effect of outflow boundary on localized initiation and rapid enhancement of severe convection over Beijing–Tianjin–Hebei region, Chinese Journal of Atmospheric Sciences, 41, 897–917, https://doi.org/10.3878/j.issn.1006-9895.1702.16101, 2017 (in Chinese).

Chen, S. H. and Lin, Y. L.: Effects of moist Froude number and CAPE on a conditionally unstable flow over a mesoscale mountain ridge, J. Atmos. Sci., 62, 331–350, 2005.

Chu, C. M. and Lin, Y. L.: Effects of orography on the generation and propagation of mesoscale convective systems in a two-dimensionally conditionally unstable flow, J. Atmos. Sci., 57, 3817–3837, 2000.

Dou, J., Wang, Y., Bornstein, R., and Miao, S.: Observed spatial characteristics of Beijing urban climate impacts on summer thunderstorms, J. Appl. Meteorol. Clim., 54, 94–104, https://doi.org/10.1175/JAMC-D-13-0355.1., 2015.

Feng, Z., Houze, R. A., Leung, L. R., Song, F., Hardin, J. C., Wang, J., Gustafson, W. I., and Homeyer, C. R.: Spatiotemporal characteristics and large-scale environments of mesoscale convective systems east of the Rocky Mountains, J. Climate, 32, 7303–7328, 2019.

Frame, J. W. and Markowski, P.: The interaction of simulated squall lines with idealized mountain ridges, Mon. Weather Rev., 134, 1919–1941, https://doi.org/10.1175/MWR3157.1, 2006.

Guo, J., Chen, X., Su, T., Liu, L., and Zhai, P.: The climatology of lower tropospheric temperature inversions in China from radiosonde measurements: roles of black carbon, local meteorology, and large-scale subsidence, J. Climate, 33, 9327–9350, https://doi.org/10.1175/JCLI-D-19-0278.1, 2020.

Guo, J., Liu, B., Gong, W., Shi, L., Zhang, Y., Ma, Y., Zhang, J., Chen, T., Bai, K., Stoffelen, A., de Leeuw, G., and Xu, X.: Technical note: First comparison of wind observations from ESA's satellite mission Aeolus and ground-based radar wind profiler network of China, Atmos. Chem. Phys., 21, 2945–2958, https://doi.org/10.5194/acp-21-2945-2021, 2021 (data available at: https://data.cma.cn, last access: 11 January 2024).

Guo, X., Guo, J., Zhang, D. L., and Yun, X.: Vertical divergence profiles as detected by two wind profiler mesonets over East China: implications for nowcasting convective storms, Q. J. Roy. Meteor. Soc., 149, 1629–1649, https://doi.org/10.1002/qj.4474, 2023.

Hersbach, H., Bell, B., Berrisford, P., Hirahara, S., Horányi, A., Muñoz-Sabater, J., Nicolas, J., Peubey, C., Radu, R., Schepers, D., Simmons, A., Soci, C., Abdalla, S., Abellan, X., Balsamo, G., Bechtold, P., Biavati, G., Bidlot, J., Bonavita, M., De Chiara, G., Dahlgren, P., Dee, D., Diamantakis, M., Dragani, R., Flemming, J., Forbes, R., Fuentes, M., Geer, A., Haimberger, L., Healy, S., Hogan, R. J., Hólm, E., Janisková, M., Keeley, S., Laloyaux, P., Lopez, P., Lupu, C., Radnoti, G., de Rosnay, P., Rozum, I., Vamborg, F., Villaume, S., and Thépaut, J.-N.: The ERA5 global reanalysis, Q. J. Roy. Meteor. Soc. 146, 1999–2049, https://doi.org/10.1002/qj.3803, 2020.

Hoffmann, L., Günther, G., Li, D., Stein, O., Wu, X., Griessbach, S., Heng, Y., Konopka, P., Müller, R., Vogel, B., and Wright, J. S.: From ERA-Interim to ERA5: the considerable impact of ECMWF's next-generation reanalysis on Lagrangian transport simulations, Atmos. Chem. Phys., 19, 3097–3124, https://doi.org/10.5194/acp-19-3097-2019, 2019.

Huang, X. M., Hu, C. Q., Huang, X., Chu, Y., Tseng, Y., Zhang, G. J., and Lin, Y. L.: A long-term tropical mesoscale convective systems dataset based on a novel objective automatic tracking algorithm, Clim. Dynam., 51, 3145–3159, https://doi.org/10.1007/s00382-018-4071-0, 2018.

Jeevanjee, N. and Romps, D. M.: Effective buoyancy, inertial pressure, and the mechanical generation of boundary layer mass flux by cold pools. J. Atmos. Sci., 72, 3199–3213, 2015.

Kang, Y., Peng, X., Wang, S., Hu, Y., and Lu, S.: Observational analyses of topographic effects on convective systems in an extreme rainfall event in northern China, Atmos. Res., 229, 127–144, https://doi.org/10.1016/j.atmosres.2019.05.024, 2019.

Keighton, S., Jackson, J., Guyer, J., and Peters, J.: A preliminary analysis of severe quasi-linear mesoscale convective systems crossing the Appalachians, Preprints, 22nd Conf. on Weather Analysis and Forecasting, Park City, UT, 27 June 2007, American Meteorological Society, P2.18, https://www.weather.gov/media/rnk/research/MCS_Appalachians_Manuscript_final.pdf (last access: 2 February 2024), 2007.

Kingsmill, D. E.: Convection initiation associated with a sea-breeze front, a gust front, and their collision, Mon. Weather Rev., 123, 2913–2933, 1995.

Lee, J. L., Browning, G. L., and Xie, Y. F.: Estimating divergence and vorticity from the wind profiler network hourly wind measurements, Tellus A, 47, 892–910, https://doi.org/10.1034/j.1600-0870.1995.00127.x, 1995.

Letkewicz, C. E. and Parker, M. D.: Forecasting the maintenance of mesoscale convective systems crossing the Appalachian Mountains, Weather Forecast., 25, 1179–1195, 2010.

Letkewicz, C. E. and Parker, M. D.: Impact of environmental variations on simulated squall lines interacting with terrain, Mon. Weather Rev., 139, 3163–3183, 2011.

Li, H., Cui, X., and Zhang, D. L.: On the initiation of an isolated heavy-rain-producing storm near the central urban area of Beijing metropolitan region, Mon. Weather Rev., 145, 181–197, https://doi.org/10.1175/MWR-D-16-0115.1, 2017.

Liu, B., Ma, Y., Guo, J., Gong, W., Zhang, Y., Li, J., Guo, X., and Shi, Y.: Boundary layer heights as derived from ground-based radar wind profiler in Beijing, IEEE T. Geosci. Remote, 57, 8095–8104, https://doi.org/10.1109/TGRS.2019.2918301, 2019.

Machado, L. A. T., Rossow, W. B., Guedes, R. L., and Walker, A. W.: Life cycle variations of mesoscale convective systems over the Americas, Mon. Weather Rev., 126, 1630–1654, 1998.

McCaul, E. W. and Cohen, C.: The initiation, longevity, and morphology of simulated convective storms as a function of free-tropospheric relative humidity, Preprints, 22nd Conf. on Severe Local Storms, Hyannis, MA, 6 October 2004, Amer. Meteor. Soc., 8A.5, https://ams.confex.com/ams/11aram22sls/webprogram/Paper81251.html (last access: 5 February 2024), 2004.

Meng, Z., Yan, D., and Zhang, Y.: General features of squall lines in East China, Mon. Weather Rev., 141, 1629–1647, https://doi.org/10.1175/MWR-D-12-00208.1, 2013.

Miglietta, M. M. and Rotunno, R.: Numerical simulations of conditionally unstable flows over a mountain ridge, J. Atmos. Sci., 66, 1865–1885, 2009.

Parker, M. D. and Ahijevych, D. A.: Convective episodes in the east-central United States, Mon. Weather Rev., 135, 3707–3727, 2007.

Qin, R. and Chen, M.: Impact of a front–dryline merger on convection initiation near a mountain ridge in Beijing, Mon. Weather Rev., 145, 2611–2633, https://doi.org/10.1175/MWR-D-16-0369.1, 2017.

Reeves, H. D. and Lin, Y. L.: The effects of a mountain on the propagation of a preexisting convective system for blocked and unblocked flow regimes, J. Atmos. Sci., 64, 2401–2421, 2007.

Rotunno, R., Klemp, J. B., and Weisman, M. L.: A theory for strong, long-lived squall lines, J. Atmos. Sci., 45, 463–485, 1988.

Sun, J. and Cheng, G.: Influence of thermal and dynamical conditions over Beijing city area on strength of down-to-hill thunderstorms, Plateau Meteorology, 36, 207–218, 2017.

Teng, J.-H., Chen, C.-S., Wang, T.-C. C., and Chen, Y.-L.: Orographic effects on a squall line system over Taiwan, Mon. Weather Rev., 128, 1123–1138, https://doi.org/10.1175/1520-0493(2000)128<1123:OEOASL>2.0.CO;2, 2000.

Tompkins, A. M.: Organization of tropical convection in low vertical wind shears: The role of water vapor, J. Atmos. Sci., 58, 529–545, https://doi.org/10.1175/1520-0469(2001)058<0529:OOTCIL>2.0.CO;2, 2001.

Wang, J., Zhang, M., Ren, S., Wang, X., and Miao, C.: Simulation study on the impact of Taihang Mountain slopes on downhill front cyclone rainstorm, Advances in Earth Science, 34, 717–730, https://doi.org/10.11867/j.issn.1001-8166.2019.07.0717, 2019.

Weckwerth, T. M.: The effect of small-scale moisture variability on thunderstorm initiation, Mon. Weather Rev., 128, 4017–4030, 2000.

Weckwerth, T. M., Bennett, L. J., Miller, L. J., Baelen, J. V., Girolamo, P. D., Blyth, A. M., and Hertneky, T. J.: An observational and modeling study of the processes leading to deep, moist convection in complex terrain, Mon. Weather Rev., 142, 2687–2708, 2014.

Wilson, J. W., Chen, M. X., and Wang, Y. C.: Nowcasting thunderstorms for the 2008 summer Olympics, The 33rd International Conference on radar Meteorology, Cairns, QLD, Australia, 10 August 2007, American Meteorological Society, 12, https://ams.confex.com/ams/33Radar/techprogram/paper_123018.htm (last access: 6 February 2024), 2007.

Wilson, J. W., Feng, Y., Chen, M., and Roberts, R. D.: Nowcasting challenges during the Beijing Olympics: Successes, failures, and implications for future nowcasting systems, Weather Forecast., 25, 1691–1714, https://doi.org/10.1175/2010WAF2222417.1, 2010.

Wu, Y., Guo, J., Chen, T., and Chen, A.: Forecasting Precipitation from Radar Wind Profiler Mesonet and Reanalysis Using the Random Forest Algorithm, Remote Sens.-Basel, 15, 1635, https://doi.org/10.3390/rs15061635, 2023.

Xiao, X., Chen, M. X., Gao, F., and Wang, Y.: A thermodynamic mechanism analysis on enhancement or dissipation of convective systems from the mountains under weak synoptic forcing, Chinese Journal of Atmospheric Sciences, 39, 100–124, 2015 (in Chinese).

Xiao, X, Sun, J., Chen, M. X., Qie, X., Wang, Y., and Ying, Z. M.: The characteristics of weakly forced mountain-to-plain precipitation systems based on radar observations and high-resolution reanalysis, J. Geophys. Res.-Atmos., 122, 3193–3213, 2017.

Xiao, X, Sun, J., Chen, M. X., Qie, X., Ying, Z. M., Wang, Y., and Ji, L.: Comparison of environmental and mesoscale characteristics of two types of mountain-to-plain precipitation systems in the Beijing region, China, J. Geophys. Res.-Atmos., 124, 6856–6872, 2019.

Yang, X. L., Sun, J. H., and Zheng, Y. G.: A 5-yr climatology of severe convective wind events over China, Weather Forecast., 32, 1289–1299, https://doi.org/10.1175/WAF-D-16-0101.1, 2017.

Zhang, D.-L.: Rapid urbanization and more extreme rainfall events, Sci. Bull., 65, 516–518, https://doi.org/10.1016/j.scib.2020.02.002, 2020.